



# Pitting and Localized Galvanic Corrosion Characteristics of Gas Tungsten Arc Welded Austenitic Stainless Steel

Seunghyun Kim<sup>1</sup> · Gidong Kim<sup>1</sup> · Chang-Young Oh<sup>1</sup> · Sangwoo Song<sup>1</sup>

Received: 21 November 2021 / Accepted: 2 December 2021 / Published online: 25 February 2022  
© The Korean Institute of Metals and Materials 2022

## Abstract

To investigate corrosion characteristics of gas-tungsten arc welded 304L-ER308L and 316L-ER316L for dry storage canister application, electrochemical impedance spectroscopy, potentiodynamic electropolarization and double loop-electrochemical potentiokinetic reactivation techniques are exploited in 0.6 M NaCl and 0.5 M H<sub>2</sub>SO<sub>4</sub> + 0.01 M KSCN + x M NaCl solution. Microstructure analysis gave that they had dendritic ferrite in austenite matrix mainly in weld metal, and ferrite fraction of 304L-ER308L was much higher than that of 316L-ER316L due to chemical composition effects. In 0.6 M NaCl, pitting corrosion appeared in both base metal and weld for 304L-ER308L because 304L and ER308L had similar electrochemical properties. In case of 316L-ER316L, noble characteristics of 316L induced reduction of corrosion rate in 316L-ER316L but galvanic coupling between base metal and weld induced severe pitting corrosion in base metal. In the H<sub>2</sub>SO<sub>4</sub> solution, three corrosion mechanism appeared for 304L-ER308L: galvanic corrosion in ferrite–austenite; galvanic corrosion in weld–base metal; pitting corrosion in base metal when 0.6 M NaCl was added. For 316L, localized galvanic corrosion in weld–base metal only appeared.

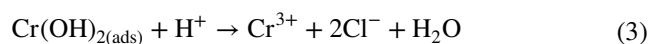
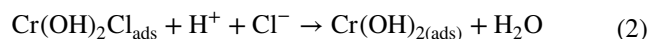
**Keywords** Chloride-induced stress corrosion cracking · Stainless steel · Weld · Pitting corrosion · Galvanic corrosion

## 1 Introduction

Worldwide demands on the interim storage of spent nuclear fuels arise due to the limited capacity of in-reactor storage [1–3]. Because of radiation and decay heat from the spent nuclear fuels, after short-term storage in the in-reactor storage, the fuels transported to an interim storage [4]. Two types, wet and dry storage, have been considered but owing to the technical and economic benefit, dry storage canister is now considered as promising system [5].

Candidate material for the dry storage canister is austenitic stainless steel such as 304L and 316L because of its excellence in corrosion resistance, mechanical properties and weldability [6–9]. However, as the system would be installed in sea- or lake-shore, chloride-induced stress corrosion cracking (CISCC) is now considered as potential degradation mechanism [4, 10, 11]. CISCC usually occurs at the weld of stainless steel with the deliquescence of salt.

Incorporation of chloride into a passive film by replacing the oxygen ions induces the dissolution of Cr oxide as follows [12]:



Since chloride induces breakdown of passivity of stainless steels, the above process stimulates pitting corrosion at the susceptible region. Eventually, initiation and propagation of crack occur at the pit, which is called pit-to-crack transition [13]. After the transition, CISCC propagates either intergranular or transgranular morphology. Thus, it is essential to evaluate pitting and intergranular corrosion characteristics of stainless steels in various saline as a precursor to CISCC behavior.

Previous works on corrosion characteristics of austenitic stainless steel welds provides that corrosion resistance in weld is superior than that of heat affected zone (HAZ) and base metal due to lower chemical composition of C, P and S

✉ Seunghyun Kim  
skims@kims.re.kr

<sup>1</sup> Joining Technology Department, Korea Institute of Materials Science, Changwon 51508, Republic of Korea

[15]. When  $\delta$ -ferrite is the primary solidification phase, the boundary area between  $\delta$ -ferrite and austenite acts as a sink for P and S. Similar trend is also reported by Zhu [16]. In his work, no obvious pitting occurs in the weld in immersion test conducted in 6% FeCl<sub>3</sub> solution. In contrast, works from Jijun point out that weld is much susceptible for corrosion due to composition segregation [17]. Also, that of C. Garcia suggest that corrosion rate of weld is higher but wider passive region appears due to Mo and Ni composition for 304L [18]. There is heavy dependency between weld corrosion resistance and Mo segregation [19]. And, the higher content of  $\delta$ -ferrite in the fusion line can be detrimental because of its susceptibility to attack in chloride media. In case of 316L,  $\delta$ -ferrite promotes Cr-depleted zone and it can be preferential corrosion attack site. Potentiodynamic studies from Otake reported that selective dissolution of austenite is observable in NaCl solution but there is no clear evident of pit initiation [20]. Recent studies on laser welded austenitic stainless steels shows that heterogenous microstructure (ferrite and austenite) induces galvanic coupling between two phases [21]. Some studies have been carried out electrochemical tests in 0.5 M H<sub>2</sub>SO<sub>4</sub> + 0.01 M KSCN + x M NaCl solution for susceptibility evaluation of stainless steels to stress corrosion cracking, pitting corrosion and intergranular corrosion [12, 14]. In summary, previous works on corrosion characteristics of austenitic stainless steel weld pointed out that local chemical composition (e.g., Cr, Mo, Ni, P and S) and phase boundaries conditions gravely makes significant effects but still in debate.

In this study, two welded plates made of 304L-ER308L and 316L-ER316L are prepared by gas tungsten arc weld (GTAW) method. And their corrosion characteristics are evaluated using direct current and alternative current based electrochemical techniques: electrochemical impedance spectroscopy (EIS), potentiodynamic electropolarization (polarization) and double loop-electrochemical potentiokinetic reactivation (DL-EPR) tests in 0.6 M NaCl and 0.5 M H<sub>2</sub>SO<sub>4</sub> + 0.01 M KSCN + x M NaCl. The test results in 0.6 M NaCl is for the purpose of characterization of the pitting corrosion in seawater since the canister would be installed in sea- or lake-shore. Furthermore, electrochemical tests in 0.5 M H<sub>2</sub>SO<sub>4</sub> + 0.01 M KSCN + x M NaCl is to investigate intergranular corrosion susceptibility in grain or phase boundaries in the austenitic stainless steels since

potential CISCC propagation path is grain boundary [22]. And the tested surface is characterized by scanning electron microscopy (SEM) and a phase-array based surface roughness analyzer.

## 2 Materials and Method

### 2.1 Preparation of the Materials

304L and 316L plates were prepared as base metal. And, ER308L and ER316L is used as weld metal for 304L and 316L, respectively. The chemical composition and Cr, Ni equivalent (Cr<sub>eq</sub>, Ni<sub>eq</sub>, respectively) of each material is given in Table 1. Cr<sub>eq</sub> and Ni<sub>eq</sub> are calculated as follows:

$$\text{Cr}_{\text{eq}} = \% \text{Cr} + \% \text{Mo} + 1.5 \times \% \text{Si} + 0.5 \times \% \text{Nb} + 2 \times \% \text{Ti} \quad (4)$$

$$\text{Ni}_{\text{eq}} = \% \text{Ni} + 30 \times \% \text{C} + 0.5 \times \% \text{Mn} \quad (5)$$

where %X indicates the wt.% of each elements. For the welding of plates, automated GTAW was used with Ar shield gas: the weldment has 24 passes not exceeding 175 °C for each passes. Maximum heat input was limited to 16.78 kJ/cm. And, geometry and photographs of the welded plates are given in Fig. 1. As shown in Fig. 1a, the size of the weld plate was 500 × 300 × 10(T) mm<sup>3</sup> and the length of the root gap was 10 mm. Figure 1b and c show the photographs of the welded plate and the weldment. Figure 1d shows the geometry of the corrosion specimen after etching, which is indicated in Fig. 1a with a red circle. The test specimens were mechanically polished using SiC papers up to 2000 grits and diamond and silica suspension (~0.25 μm). The polished specimens were sequentially rinsed in acetone–ethanol–deionized water.

### 2.2 Electrochemical Tests

Multiple electrochemical techniques were introduced to evaluate the corrosion characteristics of base metal (BM) and weld-base metal (W-BM) interface. Gamry Reference 600+ was used as a potentiostat and impedance analyzer. As test electrolytes, seawater (0.6 M NaCl) and sulfuric acid with depassivator and NaCl (0.5 M H<sub>2</sub>SO<sub>4</sub> + 0.01 M KSCN + x M

**Table 1** Chemical composition of the base and filler metals

Materials	C	Si	Mn	P	S	Cr	Ni	Mo	N	Co	Cu	Fe	Cr <sub>eq</sub>	Ni <sub>eq</sub>
304L	0.023	0.39	1.64	0.032	0.003	18.17	8.07	0.12	0.073	0.22	0.24	Bal	18.88	9.58
ER308L	0.011	0.34	1.65	0.018	0.006	19.84	10.42	0.045		0.012	0.084	Bal	20.40	11.58
316L	0.021	0.50	1.27	0.029	0.002	16.67	10.07	2.04	0.071	0.21	0.29	Bal	19.60	11.47
ER316L	0.01	0.59	1.54	0.023	0.001	18.72	11.60	2.58	0.040		0.17	Bal	22.19	12.67

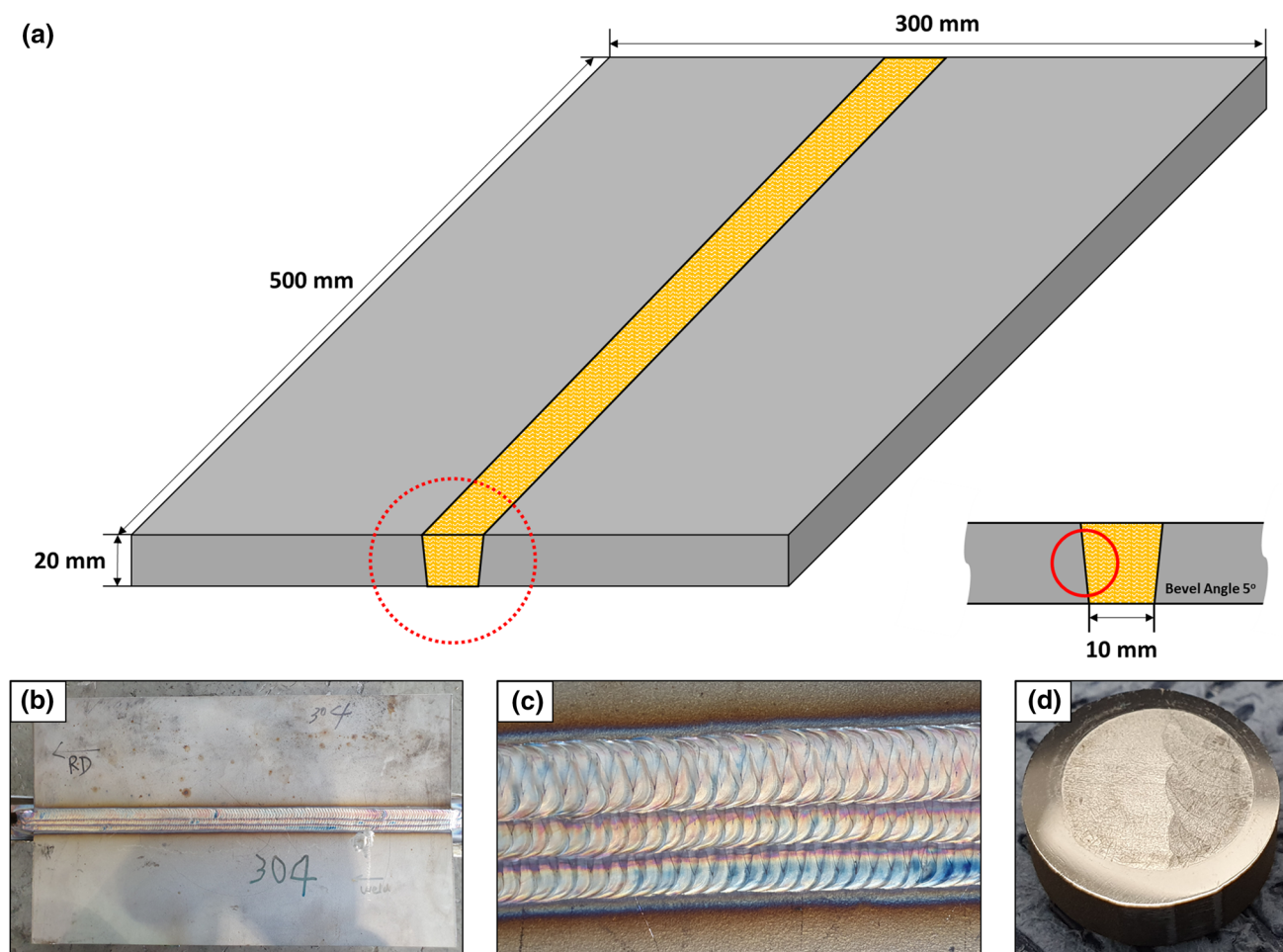


**Fig. 1** Geometry and photographs of the welded plates: **a** geometry of the welded plates, weld, and corrosion specimens, a photograph of **b** the plate, **c** the bead, and **d** the corrosion specimen after etching

NaCl ( $x=0, 0.3, 0.6$ ) were prepared [23–25]. Total cell volume of the corrosion cell was *c.a.* 500 mL and the electrolyte was refreshed after a test. For the tests, three-electrode system was configured: a corrosion specimen as a working electrode; graphite as a counter electrode; saturated KCl-filled Ag/AgCl as a reference electrode. As working electrodes, four types of specimen were prepared: 304L BM, 316L BM, 304L-ER308L W-BM interface (304L W-BM, hereafter), and 316L-ER316L W-BM interface (316L W-BM, hereafter). All the experiments were conducted after 1 h (0.6 M NaCl) or 2 min (0.5 M  $H_2SO_4$  + 0.01 M KSCN +  $x$  M NaCl) immersion in test electrolytes and open circuit potential (OCP) was measured to confirm the stability of the cell. After the measurement, EIS was conducted at 0 V vs. OCP. DC amplitude was 10 mV and frequency was swept from  $10^6$  to  $10^{-2}$  Hz. The fitting of EIS plots were carried out using Gamry Echem Analyst using trial-and-error

based Levenberg–Marquardt algorithm. Followed by EIS measurement, polarization test was carried out. The potential sweep range was  $-0.5$  V to  $1.5$  V vs. OCP with scan rate 0.833 mV/s. Sweeping of potential in DL-EPR was set as follows: initial potential at 0 V vs. OCP; apex potential at 0.5 V vs. Ag/AgCl; final potential at  $-0.3$  V vs. OCP with scan rate of 0.833 mV/s.

#### Microstructure and Chemical Analysis.

Microstructure and chemistry of the corrosion surface was carried out using SEM (IT-300, JEOL) with the attached energy dispersive X-ray microscope (EDS). EBSD analysis was also carried out to investigate the microstructure and phase fraction of the welded region (Quanta 3D FEG, FEI). Furthermore, phase-array based 3D scanning on surface roughness (Surfview, GLTECH) was carried out after corrosion tests.



### 3 Results and Discussion

#### 3.1 Materials Characterization on the W-BM interfaces

Prior to the corrosion tests, the microstructure of the specimen is analyzed by SEM, EDS, and EBSD (inverse pole figure) as shown in Fig. 2. SEM observation on 304L-ER308L in Fig. 2a shows dendritic formation of  $\delta$ -ferrite mainly in weld metal. EBSD analysis gives random distribution of grain orientation and columnar growth of grains in the weld zone as shown in Fig. 2b. Also, Fig. 2b gives that ferrite fraction in 304L-ER308L is 0.213. In case of 316L-ER316L as illustrated in Fig. 2c and d, columnar growth of grains and distribution of  $\delta$ -ferrite dendrite in weld zone likewise to those of 304L-ER308L are observable. However, the  $\delta$ -ferrite content is much smaller than that of 304L-ER308L as EBSD results gives that the ferrite fraction is 0.095. Much lower ferrite fraction of 316L-ER316L compared to 304L-ER308L is due to high  $Ni_{eq}$  in 316L and ER316L as

enlisted in Table 1 [26]. In both specimens, refinement of grain near HAZ is not observable.

#### 3.2 Corrosion Characteristics in Seawater

The results from series of the electrochemical tests performed in seawater (0.6 M NaCl) are illustrated in Figs. 3 and 4, and the corroded surface is observed using SEM as shown in Fig. 5. In EIS analysis, the modified Randle's circuit model [27], substituting a capacitor with a constant phase element (CPE) is used due to the surface roughness as shown in Fig. 3a. The model is configured by a solution resistance ( $R_{sol}$ ), a polarization resistance ( $R_p$ ), and a CPE for a double layer. The impedance of CPE ( $Z_{CPE}$ ) can be expressed as follows [28]:

$$Z_{CPE} = \frac{1}{(j\omega)^n Y_0} \quad (6)$$

where  $j$  is the imaginary number,  $\omega$  is the frequency,  $Y_0$  is the capacitance of the double layer and the  $n$  is the exponent

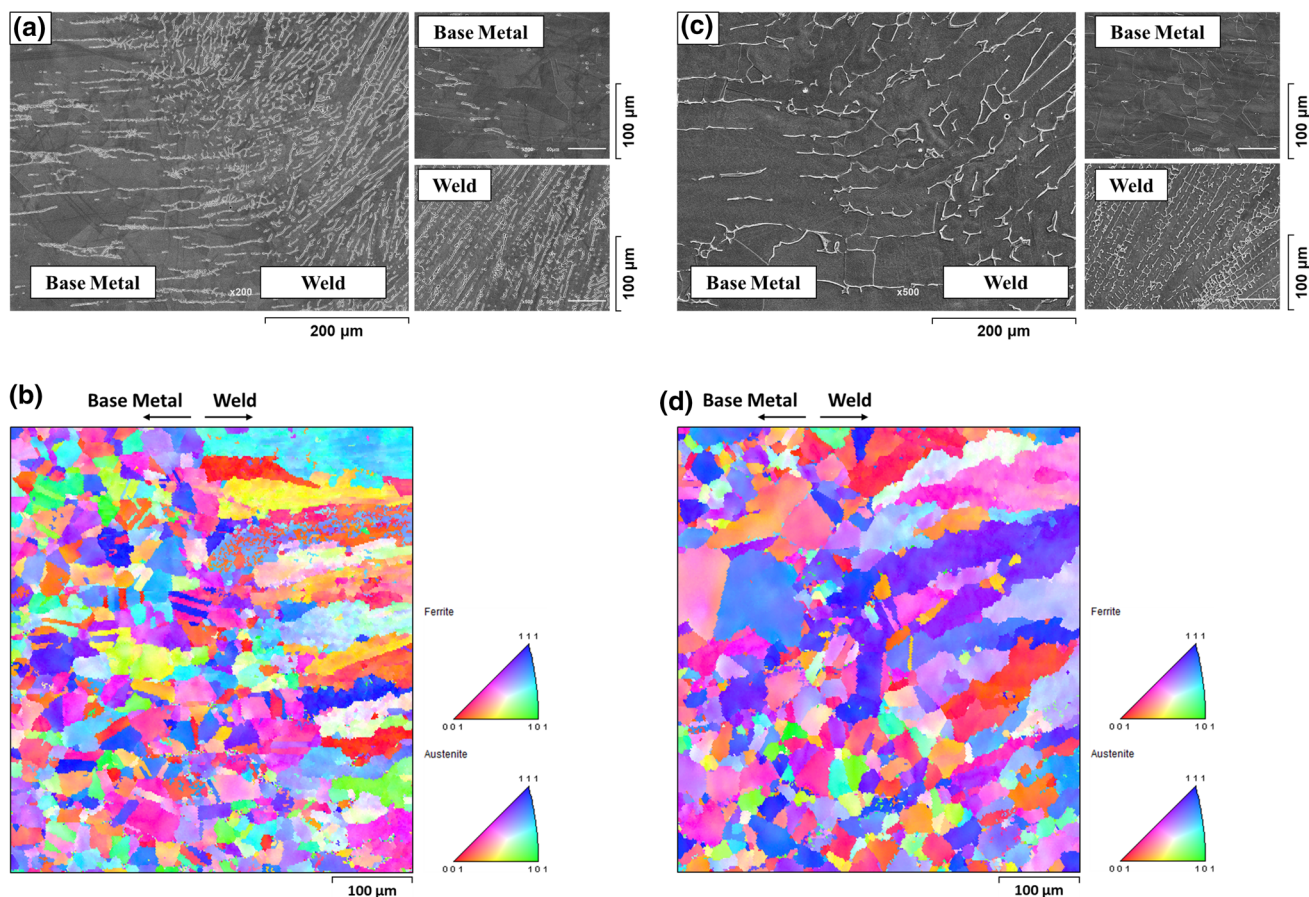


**Fig. 2** Microstructure of the weld plates: SEM images on BM, interface, and weld region of **a** 304L-ER308L and **c** 316L-ER316L; EBSD images on BM-W interface of **b** 304L-ER308L and **d** 316L-ER316L



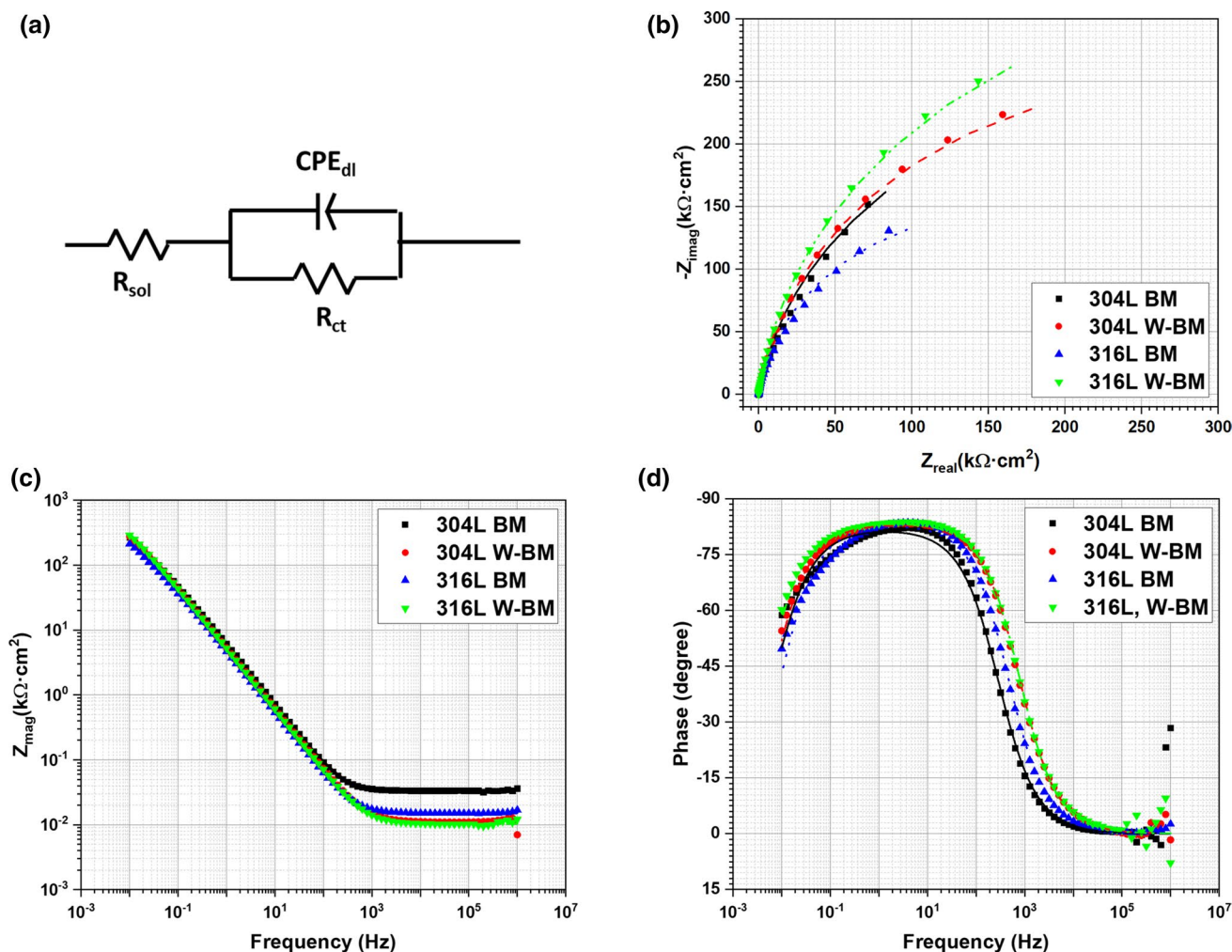


**Fig. 3** EIS results of the corrosion specimens in 0.6 M NaCl electrolyte: **a** the equivalent circuit model for the fittings; **b** Nyquist plots and **c, d** Bode plots

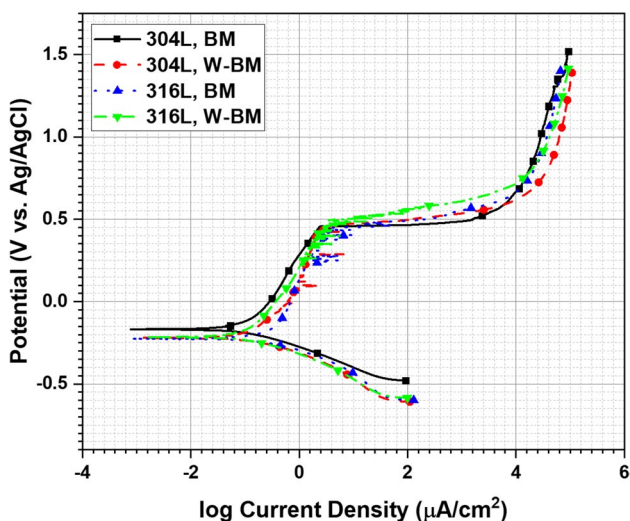


**Fig. 4** Polarization results of the corrosion specimens in 0.6 M NaCl electrolyte

equaling for 1 for an ideal capacitor. In Table 2, the fitting parameters from the EIS results are enlisted. Figure 3b gives Nyquist plots of the corrosion specimens with fitting results in straight lines. All the Nyquist plots are composed of single semi-circle indicating the corrosion kinetic matches with that of Randle's circuit model. The values of  $R_p$  of 304L BM and 304L W-BM is similar – 549.1 and 553.9  $k\Omega\text{ cm}^2$  – while those of 316L BM and 316L W-BM are 329.3 and 705.0  $k\Omega\text{ cm}^2$  respectively. This indicates that the corrosion resistance of 304L and ER308L is similar but that of ER316L is better than that of ER316L. The values of  $Y_0$  is similar with the specimen variation except 316L BM due to higher activity at the metal-electrolyte interface – higher corrosion rate. The  $n$  values are in the range of 0.911 to 0.929 indicating the double layer is analogous an ideal capacitor. In the Bode plots (Fig. 3c, d), the similar tendencies are observable. In high frequency, the effect of

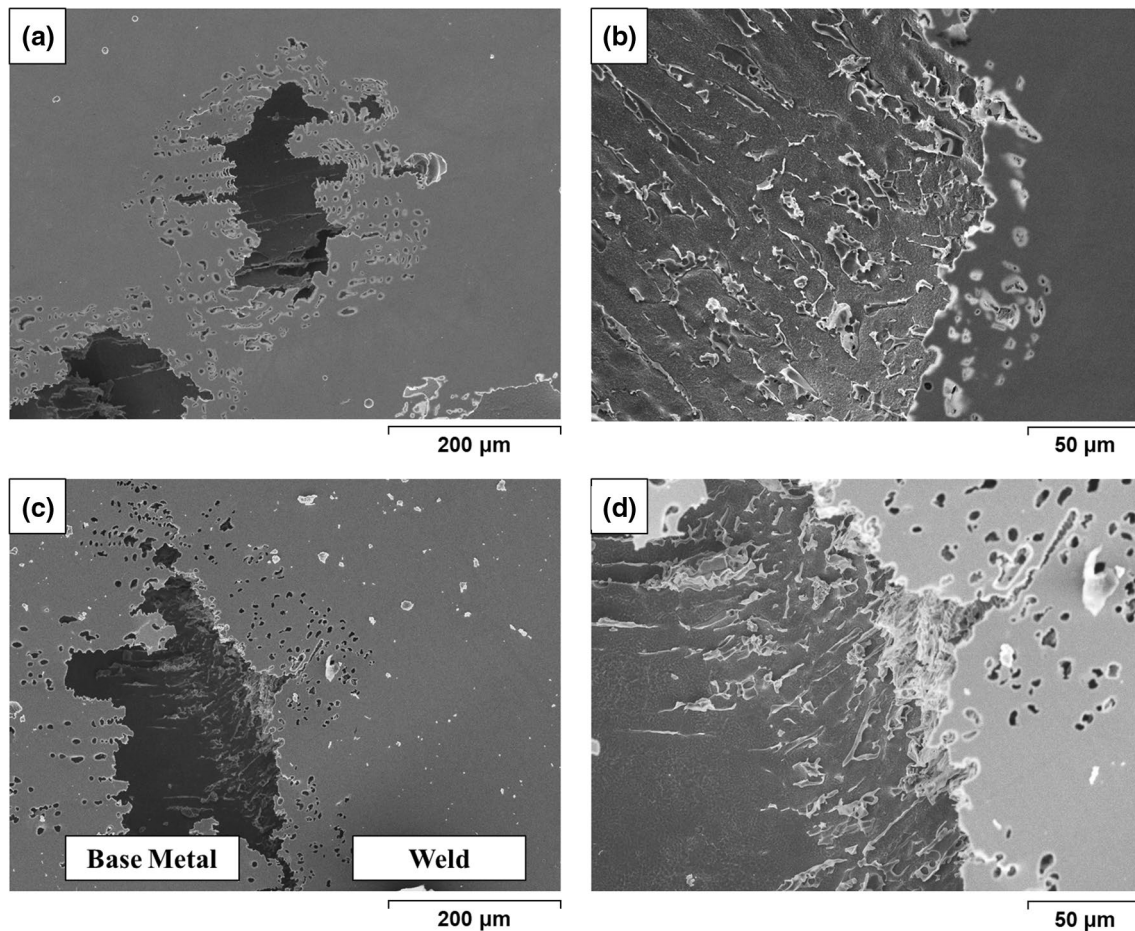


**Fig. 5** Surface morphologies of the corrosion specimen after the electrochemical tests in 0.6 M NaCl: **a, b** 304L and **c, d** 316L W-BM interfaces

**Table 2** EIS fitting parameters of the corrosion specimens in 0.6 M NaCl

	$R_{sol}$ ( $\Omega \text{ cm}^2$ )	$R_p$ ( $k\Omega \text{ cm}^2$ )	$Y_0$ ( $\mu\text{S s}^n/\text{cm}^2$ )	$n$
304L, BM	33.02	549.1	32.80	0.911
304L, W-BM	10.86	553.9	35.46	0.924
316L, BM	15.09	329.3	41.58	0.924
316L, W-BM	10.38	705.0	35.71	0.929

$R_p$  is dominant, and as frequency goes low to the phase shift from resistance to capacitor can be observable.

The polarization plots of the corrosion specimen are given in Fig. 4 with the Tafel's fitting results given in Table 3. From the fitting results, the corrosion current density ( $i_{corr}$ ), the corrosion potential ( $E_{corr}$ ), and the anodic and the cathodic Tafel slopes ( $\beta_a$ ,  $\beta_c$ ) are achieved. Comparing 304L BM and 304L W-BM, elevation of  $i_{corr}$  and shift of  $E_{corr}$  toward active region indicates that both base metal and

weld is susceptible to corrosion. In contrast, 316L W-BM exhibits better corrosion resistance than 316L BM in terms of changes in  $i_{corr}$  and  $E_{corr}$  [16, 20]. Potential at  $100 \mu\text{A}/\text{cm}^2$  is also given for the relative comparison of pitting corrosion resistance. From the results, the corrosion rate is similar for 304L BM and 316L W-BM which matches with the result from the EIS analysis. Thus, in 0.6 M NaCl solution, early conjecture comes that 304L and ER308L are susceptible but in 316L-ER316L weld, the corrosion may be inhibited due to high Cr and Mo contents in the weld [16].

The corrosion surface (Fig. 5) gives that corrosion initiation occurs in different spots for 304L W-BM and 316L W-BM. Figure 5a shows that pitting corrosion initiates in both base metal and weld for 304L W-BM. In higher magnification image in Fig. 5b, large pits with dendrite-selected corrosion are observable [16]. When the morphology is compared with Fig. 2, it can be estimated that ferrite-austenite boundary would be initiate sites by galvanic coupling between two phases. However, in case of 316L W-BM, the initiation of the corrosion usually occurs in the base metal

**Table 3** Tafel extrapolation parameters of the corrosion specimens in 0.6 M NaCl

	$i_{\text{corr}}$ ( $\mu\text{A}/\text{cm}^2$ )	$E_{\text{corr}}$ (V vs. Ag/AgCl)	$\beta_a$ (V/decade)	$\beta_c$ (V/decade)	Potential at 100 $\mu\text{A}/\text{cm}^2$ (V vs. Ag/ AgCl)
304L BM	0.138	−0.167	0.524	0.124	0.464
304L W-BM	0.216	−0.220	0.579	0.135	0.493
316L BM	0.388	−0.225	0.904	0.135	0.493
316L W-BM	0.133	−0.214	0.481	0.115	0.569

indicating ER316L possesses better corrosion resistance than base metal. This result well matches with the electrochemical results in the previous section. Figure 5d shows the morphology of the pitting corrosion site. Be like to 304L W-BM, large and small pits can be observable. The small pits are distributed along with ferrite region: ferrite and austenite boundary can be a potential pitting site since inside the large pit ferrite is relatively not corroded.

In summary, 304L BM and 304L W-BM are susceptible to pitting corrosion in 0.6 M NaCl. Even though Cr contents of 308L is slightly higher than that of 304L, the pitting corrosion occurs in both base metal and weld. In contrast, pitting corrosion only occurs in base metal of 316L W-BM due to high Cr and Mo contents in ER316L. But it may induce galvanic corrosion in weld-base metal interface.

### 3.3 Corrosion Characteristics in Sulfuric Acid Solution

For the characterization of the intergranular corrosion characteristics, EIS, polarization, and DL-EPR is performed in 0.5 M  $\text{H}_2\text{SO}_4 + 0.01$  M KSCN solution. Figure 6 illustrates EIS results in the solution and Table 4 is the fitting parameters. Figure 6a is an equivalent circuit model which is used for the interpretation of the following plots [29]. It is composed of  $R_{\text{sol}}$ ,  $\text{CPE}_{\text{dl}}$ , charge-transfer resistance ( $R_{\text{ct}}$ ),  $R_p$ , and inductance (L). Parallel  $\text{CPE}_{\text{dl}}$  and  $R_{\text{ct}}$  is related to the response in the characteristics of uniform dissolution from the passive film and series  $R_p$  and L is related to that of the electrochemical reaction in grain boundary and/or ferrite–austenite interface [29]. As enlisted in Table 4,  $R_{\text{ct}}$ , which is related to the dissolution reaction in the passive layer, is relatively high for the 316L based specimens compared to the 304L based specimens. This is owing to the enhancement of passivity due to Mo contents in 316L [18]. And W-BM specimens shows lower  $R_{\text{ct}}$  in common, meaning the passivity is hindered in W-BM interface. And, both 304L BM and 316L BM have higher  $Y_0$  than those of W-BM specimen, indicating similar tendency. The higher corrosion resistance in the passive film is observable in conductive loop in Fig. 6b and higher impedance in Fig. 6c. In both cases,  $R_p$  for both W-BM specimens are smaller and this is

because high ferrite content in the weld–ferrite–austenite boundary is susceptible to corrosion by localized galvanic coupling.

Figure 7 and Table 5 give polarization and DL-EPR tests result for both specimens in 0.5 M  $\text{H}_2\text{SO}_4 + 0.01$  M KSCN solution. In the table,  $E_p$  is the passive potential,  $i_{\text{cc}}$  is the critical current density, and  $i_p$  is the passive current. All the fitting parameters ( $i_{\text{corr}}$ ,  $E_{\text{corr}}$ ,  $E_p$ ,  $i_{\text{cc}}$  and  $i_p$ ) show that 304L specimens are severely corroded in the solution compared to 316L specimen as shown in Fig. 7a. Comparing BMs and W-BMs,  $i_{\text{corr}}$  of BMs is slightly elevated since the solution attacks ferrite–austenite boundaries. Furthermore, there is shift of  $E_{\text{corr}}$  towards active region meaning passive film formed at lower potential since ER308L and ER316L exhibits more Cr and/or Mo contents.

In DL-EPR results, Fig. 7b, the degree of sensitization (DOS) is calculated using following equation [23, 24, 30]:

$$\text{DOS}(\%) = \frac{i_r}{i_a} \times 100 \quad (7)$$

where  $i_r$  and  $i_a$  is the current peak during the reactivation and the activation, respectively. The higher DOS indicates the intergranular corrosion susceptibility of a working electrode. As described in Table 5, all the specimens exhibit DOS less than 0.15%. This indicates that intergranular corrosion at grain boundaries is not dominant mechanism in both base metal and W-BM interface. Rather corrosion in ferrite–austenite boundaries are dominant.

### 3.4 Effects of Chloride Concentration in Sulfuric Acid Solution on Corrosion Characteristics

To investigate the effects of chloride concentration on the corrosion behavior in sulfuric acid, polarization, and DL-EPR behavior of the specimens in 0.5 M  $\text{H}_2\text{SO}_4 + 0.01$  M KSCN + x M NaCl ( $x = 0, 0.3, 0.6$ ) were investigated and illustrated in Fig. 8 and Table 6. Those fitting parameters ( $i_{\text{corr}}$ ,  $E_{\text{corr}}$ ,  $E_p$ ,  $i_{\text{cc}}$ , and  $i_p$ ) reveal that 304L W-BM is much severely corroded than 316L W-BM. And there is no significant derivation of DOS between the specimens. When 0.3 M NaCl is added in the solution, there is negligibly small



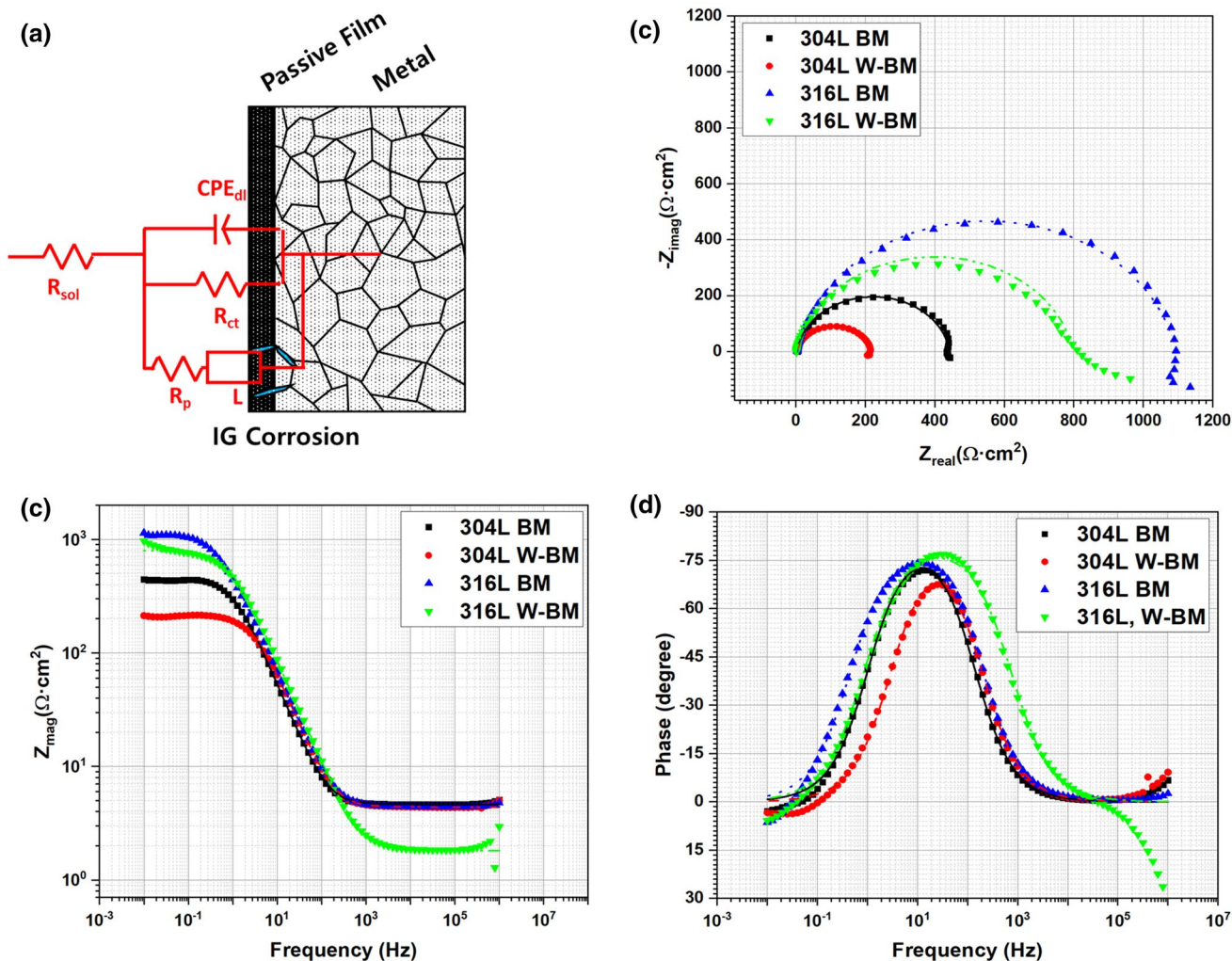


**Fig. 6** EIS results of the corrosion specimens in 0.5 M H<sub>2</sub>SO<sub>4</sub>+0.01 M KSCN electrolyte: **a** the equivalent circuit model for the fittings; **b** Nyquist plots and **c, d** Bode plots

**Table 4** EIS fitting parameters of the corrosion specimens in 0.5 M H<sub>2</sub>SO<sub>4</sub>+0.01 M KSCN

	R <sub>sol</sub> (Ω cm <sup>2</sup> )	R <sub>ct</sub> (Ω cm <sup>2</sup> )	Y <sub>0</sub> (μS s <sup>n</sup> /cm <sup>2</sup> )	n <sub>dl</sub>	R <sub>p</sub> (Ω cm <sup>2</sup> )	L (H/cm <sup>2</sup> )
304L BM	4.630	441.7	399.8	0.931	42.97 × 10 <sup>3</sup>	144.2
304L W-BM	4.389	208.2	322.6	0.927	31.13 × 10 <sup>3</sup>	88.69
316L BM	4.405	1171	354.6	0.904	15.17 × 10 <sup>3</sup>	84.22
316L W-BM	1.811	848.2	281.3	0.899	13.19 × 10 <sup>3</sup>	141.3

change in the fitting parameters in both specimens. However, when 0.6 M NaCl is added in the solution, 304L W-BM presents significant elevation in *i*<sub>corr</sub> and *E*<sub>p</sub>, *i*<sub>cc</sub> and *i*<sub>p</sub> owing to the breakaway of the passive film due to chloride. In contrast, 316L W-BM only shows slight elevation in *i*<sub>cc</sub> and *i*<sub>p</sub>.

### 3.5 Surface Morphologies After the Tests

Surface morphologies of the specimens after the polarization tests, which are conducted in the Sect. 3.4, are investigated as shown in Figs. 9 and 10. In Fig. 9a, corrosion in ferrite–austenite grain boundaries in base metal and weld are observable. Those localized galvanic corrosion is due to Cr depletion during ferrite formation [18]. Also, due to high ferrite content in the weld, the weld is corroded much

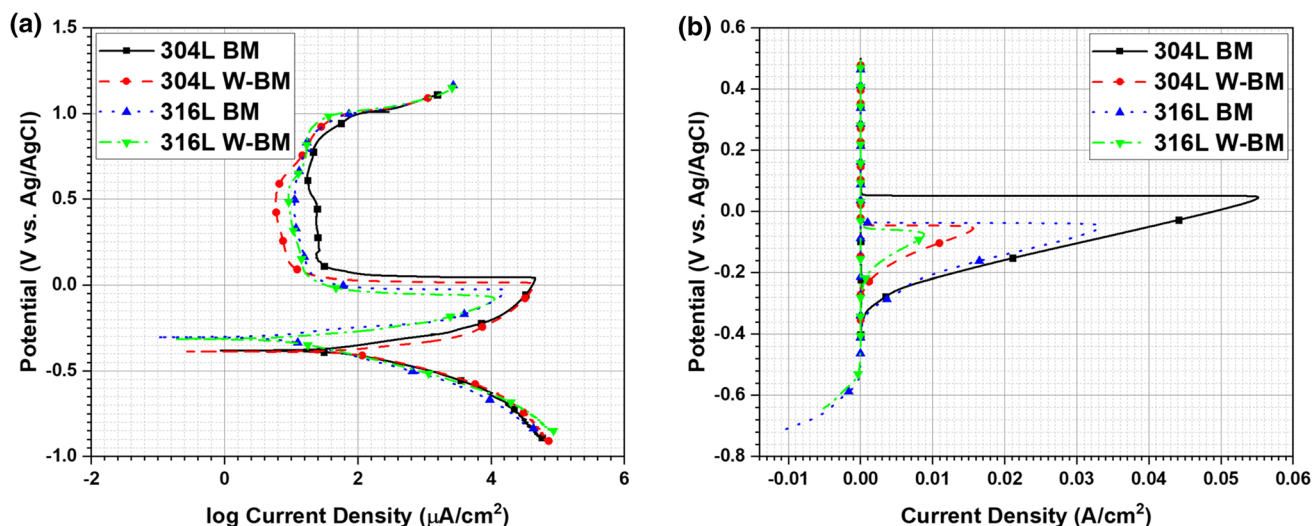


**Fig. 7** **a** Polarization and **b** DL-EPR results of the corrosion specimens in 0.5 M  $\text{H}_2\text{SO}_4 + 0.01$  M KSCN electrolyte

**Table 5** Tafel extrapolation and DL-EPR parameters of the corrosion specimens in 0.5 M  $\text{H}_2\text{SO}_4 + 0.01$  M KSCN

	$i_{\text{corr}}$ ( $\mu\text{A}/\text{cm}^2$ )	$E_{\text{corr}}$ (mV vs. Ag/ AgCl)	$\beta_a$ (mV/decade)	$\beta_c$ (mV/decade)	$E_p$ (mV vs. Ag/AgCl)	$i_{\text{cc}}$ ( $\mu\text{A}/\text{cm}^2$ )	$i_p$ ( $\mu\text{A}/\text{cm}^2$ )	DOS (%)
304L BM	83.70	-381	94.80	109.6	41.90	$46.3 \times 10^3$	24.6	0.15
304L W-BM	86.10	-387	53.20	94.90	12.97	$46.0 \times 10^3$	6.565	0.086
316L BM	5.650	-303	43.60	98.00	-24.45	$15.2 \times 10^3$	12.90	0.0061
316L W-BM	8.660	-314	48.00	94.20	-74.35	$11.0 \times 10^3$	13.00	0.0034

severely. When NaCl concentration is 0.3 M (Fig. 9b), corrosion morphology is similar but there is observation of attack in ferrite. This indicates that NaCl attacks ferrite: galvanic coupling between austenite and ferrite induces high potential difference for ferrite corrosion [6, 21]. Finally, when 0.6 M NaCl is added (Fig. 9c), pits appear in base metal region and the severe corrosion is observable in both ferrite–austenite grain boundary and ferrite itself. Thus, it can be concluded that, ferrite–austenite boundaries of 304L W-BM is susceptible corrosion site and 0.6 M NaCl induces pitting corrosion in base metal. In contrast, corrosion at the ferrite–austenite grain boundary in 316L W-BM is not observable. Even though NaCl concentration increases (from Fig. 9d–f), ferrite–austenite boundary is stable but pits initiate when NaCl concentration is 0.6 M.

In Fig. 10, the surface roughness mapping of the same corrosion specimen is illustrated. In Fig. 10a, the map of 304L W-BM after the polarization test at 0.5 M  $\text{H}_2\text{SO}_4 + 0.01$  M KSCN is given. As described in the previous paragraph, the corrosion is concentrated on ferrite–austenite grain boundary since there is clear observation of undulation in the weld. Moreover, the localized

corrosion is observable at the weld-base metal boundary. Those two phenomena are induced by galvanic coupling between two different metals or phases. In 0.5 M  $\text{H}_2\text{SO}_4 + 0.01$  M KSCN + 0.3 M NaCl (Fig. 10b), the similar tendency is observable. As NaCl concentration reaches 0.6 M (Fig. 10c), the pits initiate and the corrosion in both interfaces are observable. In case of 316L W-BM, the corrosion at the ferrite–austenite is not observable in all NaCl concentration. In 0.5 M  $\text{H}_2\text{SO}_4 + 0.01$  M KSCN solution (Fig. 10d), the main corrosion mechanism is weld-base metal interface corrosion due to the galvanic coupling. Even though NaCl concentration is 0.3 M, pits or phase interface corrosion is not observable (Fig. 10e). When NaCl concentration reaches 0.6 M (Fig. 10f), much severe corrosion at the weld-base metal interface reveals. Thus for 316L W-BM, the most critical corrosion site is near fusion line [18]. In Sect. 3.3 and 3.4, it is figured out that corrosion characteristics of 304L BM and 304L W-BM is analogous while 316L W-BM exhibits distinct characteristics compared to 316L BM. In Fig. 10, localized galvanic corrosion is much severe for 316L W-BM. Therefore, even though 316L W-BM show less corrosion

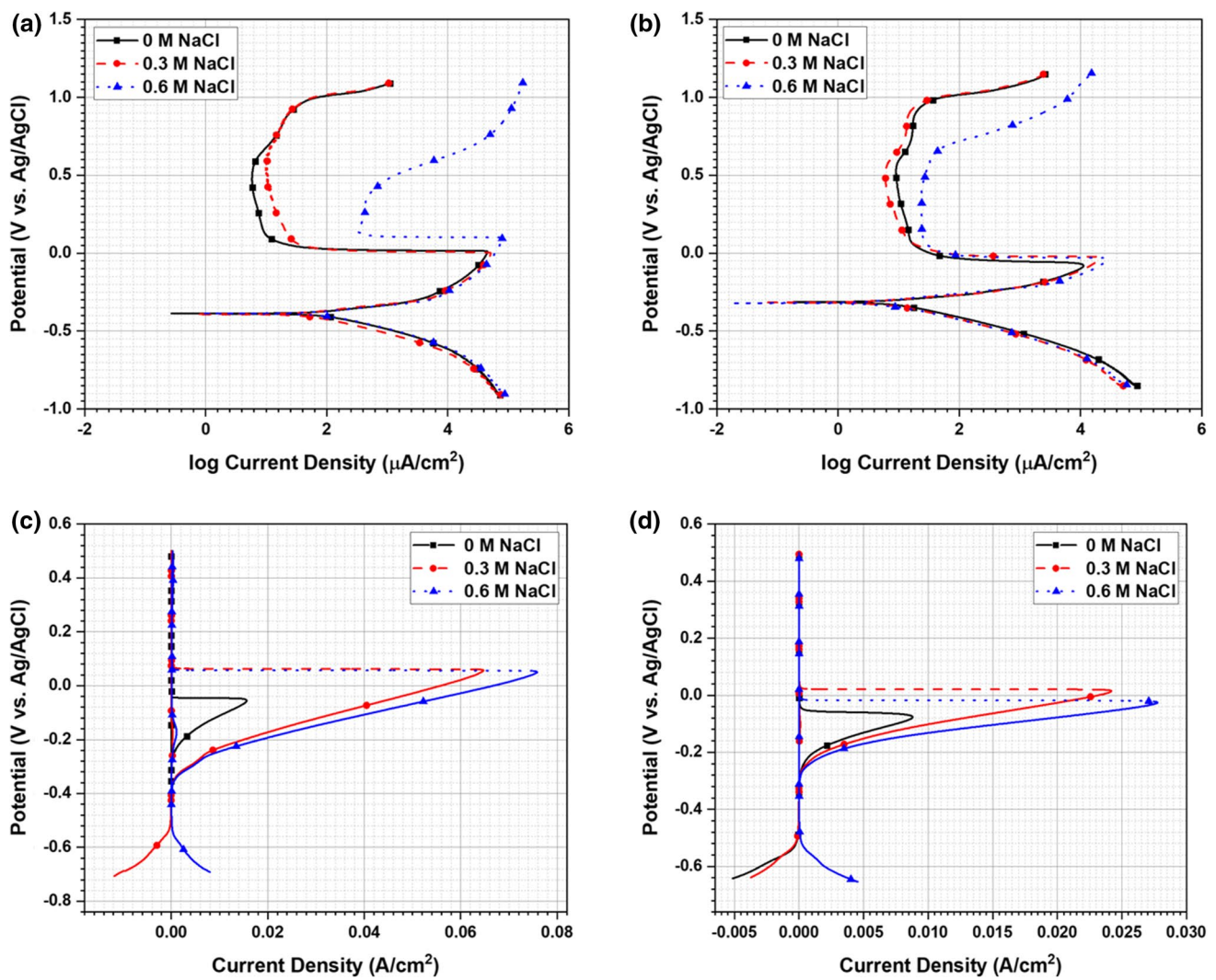


**Fig. 8** a, b Polarization, and c, d DL-EPR results of the corrosion specimens in 0.5 M H<sub>2</sub>SO<sub>4</sub> + 0.01 M KSCN + x M NaCl solutions

**Table 6** Tafel extrapolation and DL-EPR parameters of the corrosion specimens in 0.5 M H<sub>2</sub>SO<sub>4</sub> + 0.01 M KSCN + x M NaCl

	NaCl (M)	$i_{\text{corr}}$ ( $\mu\text{A}/\text{cm}^2$ )	$E_{\text{corr}}$ (mV vs. Ag/AgCl)	$\beta_a$ (mV/decade)	$\beta_c$ (mV/decade)	$E_p$ (mV vs. Ag/AgCl)	$i_{\text{cc}}$ ( $\mu\text{A}/\text{cm}^2$ )	$i_p$ ( $\mu\text{A}/\text{cm}^2$ )	DOS (%)
304L W-BM	0	86.10	-387	53.20	94.90	12.97	46.0 $\times 10^3$	6.565	0.086
	0.3	96.60	-391	83.90	131.3	7.984	49.10 $\times 10^3$	10.07	0.48
	0.6	120.0	-387	62.00	109.6	101.8	83.20 $\times 10^3$	312.2	1.48
316L W-BM	0	8.660	-314	48.00	94.20	-74.35	11.0 $\times 10^3$	13.00	0.0034
	0.3	8.970	-316	62.10	108.4	-23.95	20.62 $\times 10^3$	6.117	0.40
	0.6	7.910	-320	62.60	111.8	-31.94	27.17 $\times 10^3$	24.15	0.064



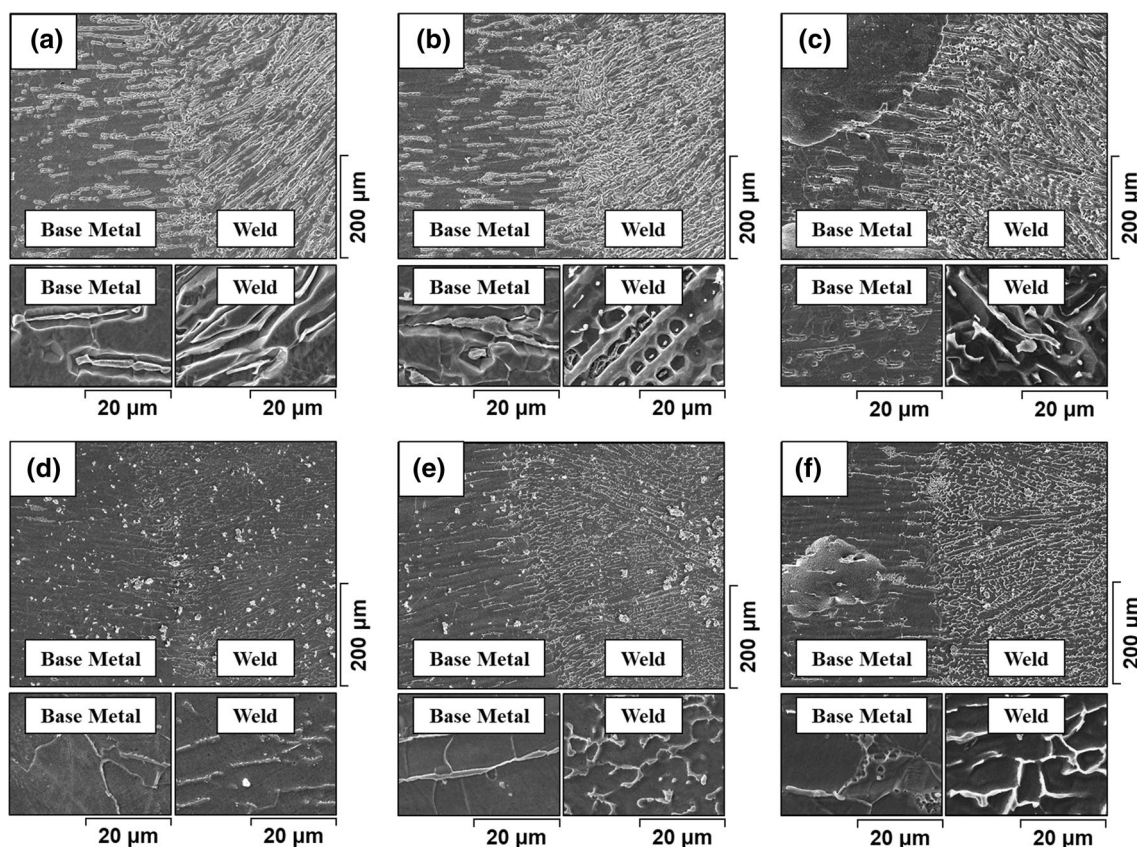


**Fig. 9** SEM images on the corrosion surface of 304L W-BM after the polarization tests in **a** 0, **b** 0.3 and **c** 0.6 M and 316L W-BM in **d** 0, **e** 0.3 and **f** 0.6 M NaCl concentration

in the corrosive environments, its localized corrosion near fusion zone should be considered.

From the followed tests, it can be concluded that 304L W-BM exhibits three corrosion mechanism as shown in Fig. 11: (1) ferrite–austenite boundary corrosion due to distinctive electrochemical characteristics between two phases, (2) weld–base metal galvanic corrosion induced by chemical composition, (3) pitting corrosion preferred in base metal.

## 4 Conclusion

In this work, two austenitic stainless steel welds made of 304L-ER308L and 316L-ER316L are prepared, and their corrosion characteristics are investigated using electrochemical techniques in 0.6 M NaCl and 0.5 M  $\text{H}_2\text{SO}_4 + 0.01$  M KSCN +  $x$  M NaCl.

(1) 304L-ER308L, 316L-ER316L have dendritic ferrite in weld zone but ferrite fraction in 304L-ER308L (0.213) is higher than that of 316L-ER316L (0.095) owing to  $\text{Cr}_{\text{eq}}$  and  $\text{Ni}_{\text{eq}}$  difference according to SEM and EBSD analysis.

- (2) In 0.6 M NaCl solution, severe pitting corrosion occurs in both base metal and weld of 304L-ER308L. Electrochemical parameters give that 304L and ER308L have similar properties thus only pitting corrosion is observable. In contrast, compared to 316L, ER316L is much nobler in the solution, thus this induces galvanic coupling in 316L-ER316L. Preferential pitting corrosion site for 316L-ER316L is base metal. This is due to high Cr and Mo contents in ER316L.
- (3) In 0.5 M  $\text{H}_2\text{SO}_4 + 0.01$  M KSCN +  $x$  M NaCl, intergranular corrosion in austenite grain boundary is not observable but severe corrosion in ferrite–austenite grain boundary is shown due to localized galvanic coupling between two phases. As NaCl concentration increases, there is pitting corrosion in base metal. Surface roughness analysis gives that there is galvanic corrosion between weld and base metal. Therefore, for 304L-ER308L three corrosion mechanism exists: galvanic corrosion in ferrite–austenite boundaries; galvanic corrosion in base metal–weld; pitting corrosion in base metal.
- (4) In the same solution, 316L-ER316L does not exhibit intergranular corrosion and localized galvanic cor-

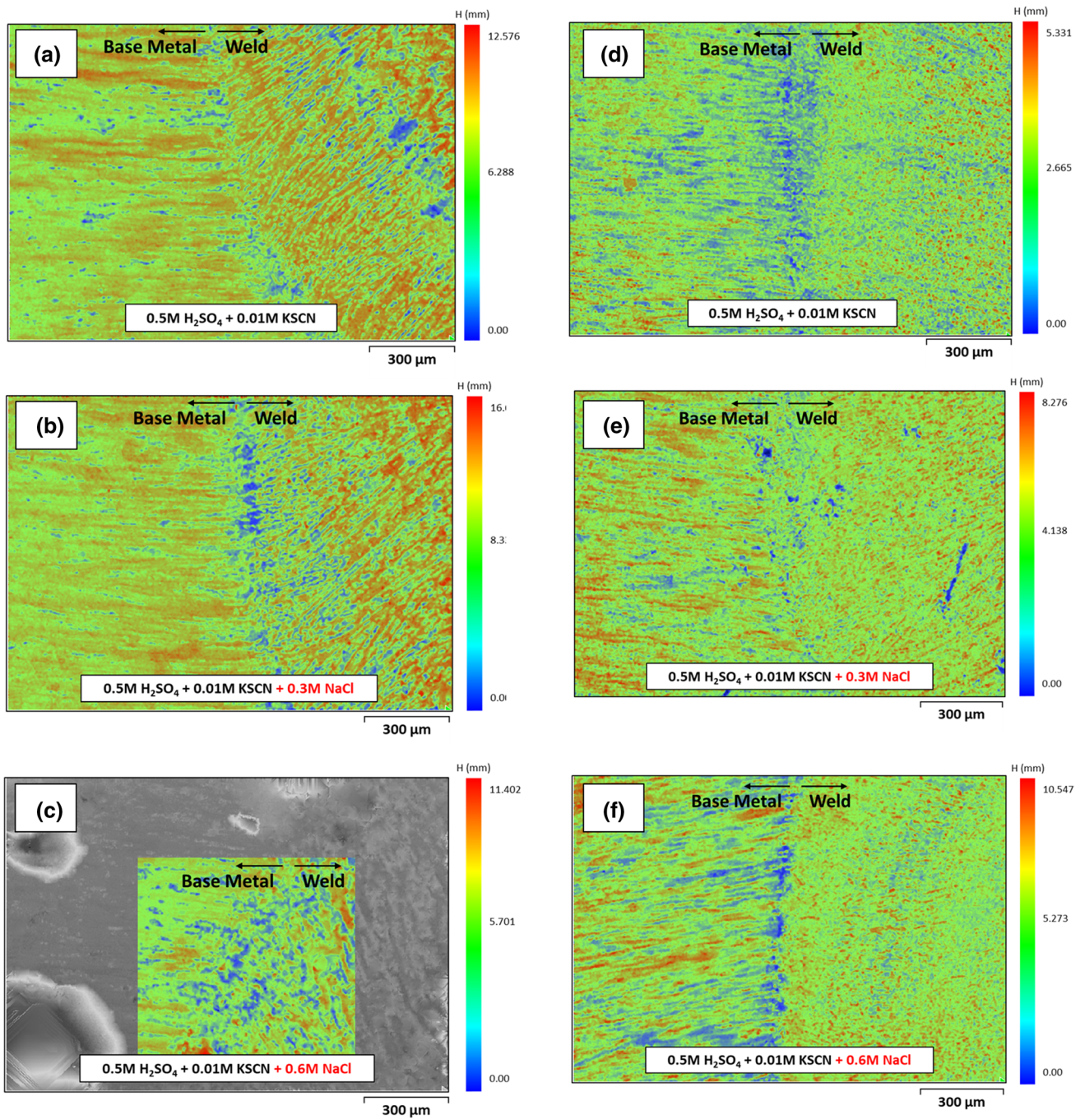


**Fig. 10** Surface roughness mapping on the corrosion surface of 304L W-BM after the polarization tests in **a** 0, **b** 0.3 and **c** 0.6 M and 316L W-BM in **d** 0, **e** 0.3 and **f** 0.6 M NaCl concentration



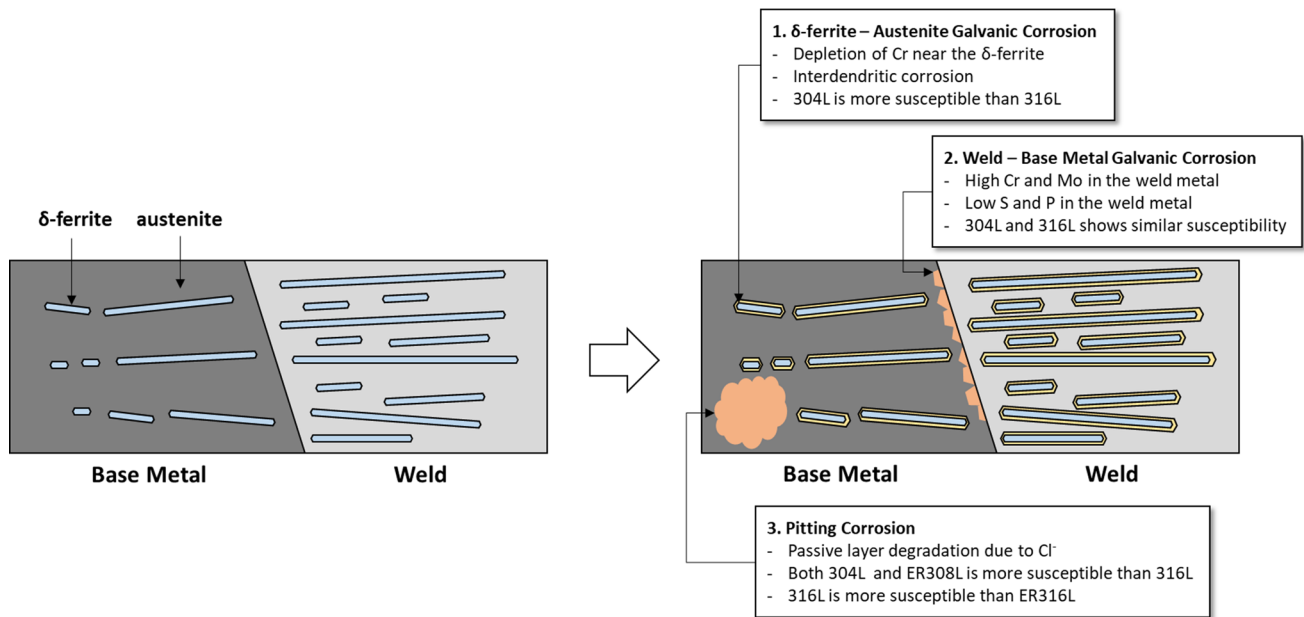


**Fig. 11** Corrosion mechanism of austenite stainless steel welds (304L-ER308L and 316L-ER316L) in chloride containing media

rosion in ferrite–austenite grain boundary. However, galvanic corrosion in weld–base metal is observable according to surface roughness analysis. Therefore, for dry storage canister application, 316L-ER316L exhibits better performance according to electrochemical tests. However, even though 316L-ER316L is utilized, potential galvanic corrosion in weld–base metal should be concerned.

**Acknowledgements** This study was supported by the Fundamental Research Program of the Korea Institute of Materials Science (PNK7530)

#### Declaration

**Competing interests** The authors whose names are listed immediately below have no relevant financial or non-financial interests to disclose.

## References

- M.G. El-Samrah, A.F. Tawfic, S.E. Chidiac, *Ann. Nucl. Energy* **160**, 108408 (2021)
- D.G. Bennett, R. Gens, *J. Nucl. Mater.* **379**, 1 (2008)
- J. Kim, D. Kook, J. Sim, Y. Kim, *J. Nucl. Fuel Cycle Waste Technol.* **11**, 333 (2013)
- Y. Xie, J. Zhang, *J. Nucl. Mater.* **466**, 85 (2015)
- L.S. Romanato, Advantages of dry hardened cask storage over wet storage for spent nuclear fuel, in *2011 International Nuclear Atlantic Conference - INAC 2011*, Belo Horizonte, Brazil, 24–28 October 2011 (Associação Brasileira de Energia Nuclear, Rio de Janeiro, 2011)
- A. Sriba, J.-B. Vogt, *Met. Mater. Int.* **27**, 5258 (2021)
- H.-Y. Huang, *Met. Mater. Int.* **16**, 819 (2010)
- C.H. Lee, *Met. Mater. Int.* **2**, 81 (1996)
- T.M. Ahn, G. Oberson, S. DePaula, *ECS Trans.* **50**, 211 (2013)
- A.J. Duncan, P.-S. Lam, R.L. Sindelar, J.T. Carter, in *Proceedings of the ASME 2017 Pressure Vessels and Piping Conference*. Volume 6B: Materials and Fabrication. Waikoloa, USA. 16–20 July 2017. V06BT06A064. (ASME, New York, 2017)
- R.L. Sindelar, J.T. Carter, A.J. Duncan, B.L. Garcia-Diaz, P.-S. Lam, B.J. Wiersma, in *Proceedings of the ASME 2016 Pressure Vessels and Piping Conference*. Volume 6B: Materials and Fabrication. Vancouver, Canada. 17–21 July 2016. V06BT06A065 (ASME, New York, 2016)
- Z.B. Wang, H.X. Hu, Y.G. Zheng, *Corros. Sci.* **130**, 203 (2018)
- X. Huang, Experimental and modelling studies of pit-to-crack transition under corrosion fatigue conditions, Ph.D. thesis, Massachusetts Institute of Technology (2017)
- R. Wang, M. Imagawa, M. Honda, T. Mori, H. Fukuhara, *Corros. Eng. Sci. Technol.* **53**, 44 (2018)
- L. Li, C.F. Dong, K. Xiao, J.Z. Yao, X.G. Li, *Constr. Build. Mater.* **68**, 709 (2014)
- P. Zhu, X. Cao, W. Wang, J. Zhao, Y. Lu, T. Shoji, *J. Mater. Res.* **32**, 3904 (2017)
- J. Xin, Y. Song, C. Fang, J. Wei, C. Huang, S. Wang, *Fusion Eng. Des.* **133**, 70 (2018)
- C. Garcia, F. Martin, P. de Tiedra, Y. Blanco, M. Lopez, *Corros. Sci.* **50**, 1184 (2008)
- P.I. Marshall, T.G. Gooch, *Corrosion* **49**, 514 (1993)
- A. Otake, I. Muto, A. Chiba, Y. Sugawara, N. Hara, *J. Electrochem. Soc.* **164**, C991 (2017)
- C.T. Kwok, S.L. Fong, F.T. Cheng, H.C. Man, *J. Mater. Process. Technol.* **176**, 168 (2006)
- B.T. Lu, Z.K. Chen, J.L. Luo, B.M. Patchett, Z.H. Xu, *Electrochim. Acta* **50**, 1391 (2005)
- J. Gong, Y.M. Jiang, B. Deng, J.L. Xu, J.P. Hu, J. Li, *Electrochim. Acta* **55**, 5077 (2010)
- K.I. Shutko, V.N. Belous, *J. Nucl. Mater.* **307–311**, 1016 (2002)



25. G.H. Aydođdu, M.K. Aydinol, *Corros. Sci.* **48**, 3565 (2006)
26. S. Kou, *Welding Metallurgy* (John Wiley & Sons, Hoboken, New Jersey, 2003)
27. J.E.B. Randles, *Discuss. Faraday Soc.* **1**, 11 (1947)
28. B. Hirschorn, M.E. Orazem, B. Tribollet, V. Vivier, I. Frateur, M. Musiani, *Electrochim. Acta* **55**, 6218 (2010)
29. K. Morshed-Behbahani, P. Najafisayar, M. Pakshir, M. Shahsavari, *Corros. Sci.* **138**, 28 (2018)
30. J.F. Rimbart, J. Pagetti, *Corros. Sci.* **20**, 189 (1980)

**Publisher's Note** Springer Nature remains neutral with regard to jurisdictional claims in published maps and institutional affiliations.